NUREG/CR-3804 Vol. II
ANL-84-35 Vol. II

NUREG/CR-3804 Vol. II
ANL-84-35 Vol. II

PHYSICS OF REACTOR SAFETY

Quarterly Report
April – June 1984

ARGONNE NATIONAL LABORATORY, ARGONNE, ILLINOIS
Operated by THE UNIVERSITY OF CHICAGO

Prepared for the Office of Nuclear Regulatory Research
U. S. NUCLEAR REGULATORY COMMISSION
under Interagency Agreement DOE 40-550-75

Argonne National Laboratory, with facilities in the states of Illinois and Idaho, is owned by the United States government, and operated by The University of Chicago under the provisions of a contract with the Department of Energy.

NUREG/CR-3804 Vol. II
ANL-84-35 Vol. II

(Distribution
Code: R7)

ARGONNE NATIONAL LABORATORY
9700 South Cass Avenue
Argonne, Illinois 60439

PHYSICS OF REACTOR SAFETY

Quarterly Report
April—June 1984

Applied Physics Division
Components Technology Division

August 1984

Previous reports in this series

ANL-83-11 (II)	April—June 1983
ANL-83-11 (III)	July—September 1983
ANL-83-11 (IV)	October—December 1983
ANL-84-35 (I)	January—March 1984

Prepared for the Division of Accident Evaluation
Office of Nuclear Regulatory Research
U. S. Nuclear Regulatory Commission
Washington, D. C. 20555
Under Interagency Agreement DOE 40-550-75

NRC FIN Nos. A2015 and A2045

PHYSICS OF REACTOR SAFETY

Quarterly Report
April-June 1984

ABSTRACT

This Quarterly progress report summarizes work done during the months of April-June 1984 in Argonne National Laboratory's Applied Physics and Components Technology Divisions for the Division of Reactor Safety Research of the U.S. Nuclear Regulatory Commission. The work in the Applied Physics Division includes reports on reactor safety modeling and assessment by members of the Reactor Safety Appraisals Section. Work on reactor core thermal-hydraulics is performed in ANL's Components Technology Division, emphasizing 3-dimensional code development for LMFBR accidents under natural convection conditions. An executive summary is provided including a statement of the findings and recommendations of the report.

FIN No.	Title
A2015	Reactor Safety Modeling and Assessment
A2045	3-D Time-dependent Code Development

TABLE OF CONTENTS

LIST OF FIGURES

LIST OF TABLES

Executive Summary

Parameter studies of pin failure for an LMFBR oxide fuel pin for LOF-TOP and 10 ¢/s TOP cases have been performed with the FPIN2 code. The pin selected for study was that for the CRBR EOC4 core. For the LOF-TOP cases intermediate and low power driver fuel was chosen. Clad failure criteria chosen were a life fraction rule using the Dorn Parameter, and also attainment of plastic hoop strain values of 0.01%, 1% and 2%. A HEDL plastic strain correlation was also used. The plastic strain value of 0.01% is in the range expected from the DiMelfi-Kramer fuel adjacency effect theory. Experimental failure strains for irradiated clad show considerable scatter but are generally in the range 0.01-1.0%.

For the Dorn Parameter and 0.01% plastic strain criteria failure tends to occur at low fuel melt fraction from mechanical interaction of fuel and clad if fuel creep is not taken into account. For large assumed failure strain, failure tends to occur from gas pressure loading at high fuel melt fraction in any case. The effect of fuel creep is very large for the 10 ¢/s TOP case, somewhat smaller for the intermediate power LOF-TOP case, and still smaller for the low power LOF-TOP case.

The BIFLO code, which is being developed for analysis of two-dimensional sodium boiling in a fuel assembly, is being used to perform a two-dimensional posttest analysis of a flow coastdown experiment performed in the OPERA Facility. The steady-state thermocouple data from the experiment show a temperature distribution which is three-dimensional and which is markedly different from the two-dimensional pattern which was expected based on the bundle design. The difference between the actual and expected temperature distribution appears to be due to movements of the bundle walls, pins, and wire wraps out of their design configurations. The bundle appears to be divisible in a manner which preserves some of the important features of the steady-state temperature distribution using three regions. Although the resulting geometry is not purely two-dimensional, BIFLO calculations are in progress to refine the details of this division of the bundle in order that the posttest analysis may proceed.

In the single-phase development work, the effort was devoted to the following three areas.

1. Free Surface Boundary Option

The modified volume of fraction approach (VOF) has been developed for implementing free surface boundary option in COMMIX-1A. Currently, in our development, we assume that the free surface in a computational cell is a horizontal surface.

The necessary modifications have been implemented. The next step is to debug and run several test problems.

2. Generalization of Semi-Implicit/Fully-Implicit Scheme

In order to merge both schemes (semi-implicit/fully-implicit) into one generalized scheme, the necessary modification effort has been initiated. A new parameter, α, has been introduced in the formulation such that

$\alpha = 0$ Semi-implicit
$\alpha = 1$ Fully-implicit
$\alpha = > 0$ and < 1 Partially-implicit

The advantage of such merging is the reduction in the size of the code plus a wide range of flexibility.

3. DRACS Analysis Capability

In the area of DRACS Analysis Capability, a third fluid option has been implemented.

In the area of two-phase development work, the efforts were continued in

1. Combining the Equilibrium model with slip (SM-HEM) and Separated phase model into one generalized model,

2. Development of a model for the calculation of evaporation (condensation) rate, and

3. Development of subroutines for the calculation of mass and energy imbalances.

I. REACTOR SAFETY MODELING AND ASSESSMENT

(A2015)

A. Fuel Pin Failure Studies with FPIN2 for an LMFBR Oxide Fuel Pin
(H. H. Hummel)

The FPIN2 code, made available in advance of general release by courtesy of the developers, T. H. Hughes and J. M. Kramer of ANL, has been used for parametric studies of failure of an LMFBR oxide fuel pin. Some features of this code were mentioned in the previous quarterly report[1]. Power histories for the assumed transients leading to pin failure are given in Table I.

TABLE I. Power Histories in LOF-TOP and TOP Pin Failure Calculations

LOF-TOP						TOP		
Channel 9			Channel 14					
Time, sec	Relative Power	Max Fuel Melt Fr[a]	Time, sec	Relative Power	Max Fuel Melt Fr[a]	Time, sec	Relative Power	Max Fuel Melt Fr[a]
0.0	1.00	0.0	0.0	1.0	0.0	0.0	1.0	0.0
14.0	1.54	0.0	14.0	1.54	0.0	2.50	1.44	0.0
14.495	3.32	0.0	14.495	3.32	0.0	5.10	1.90	0.0
14.995	9.09	0.009	14.995	9.49	0.0	6.50	2.12	0.002
15.095	13.1	0.116	15.095	11.1	0.0	7.50	2.27	0.064
15.159	18.6	0.308	15.195	19.7	0.02	8.50	2.42	0.161
15.199	20.8	0.441	15.2066	26.2	0.038	9.50	2.58	0.251
15.207	23.3	0.468	15.2089	92	0.049	10.50	2.81	0.331
			15.2104	328	0.079	11.10	3.00	0.380
			15.2116	936	0.177	11.50	3.13	0.429
			15.2124	1424	0.361	12.10	3.29	0.478
			15.2127	1600	0.476			

[a]Fuel/clad gap conductance constant at 1.14 watts/cm^2-K. Fuel/clad gap assumed closed for each node in steady-state.

Channels 9 and 14 are intermediate and low power driver fuel channels in a 15-channel representation of the CRBR EOC4 heterogeneous core. For channel 9, sodium boiling and flow reversal occur during the rise to 20 times normal power, with extensive voiding having occurred by the end of this time. For channel 14, only limited sodium voiding occurs, so that the clad stays considerably cooler. The assumed transient for channel 14 is nearly identical with that for channel 9 up to about 20 times normal power; after that there is a power rise to 1600 times normal power in a few milliseconds, corresponding to a large imposed reactivity ramp. The fuel melt fraction in channel 14 is less than that in channel 9 at a given time because of the lower steady state power. For the TOP cases a high power driver fuel channel is selected, with power rising to about 3 times normal in 12 seconds, corresponding to a reactivity ramp of about 10 ¢/s. In the FPIN2 calculations the clad outer temperatures were input as a function of time based on the results of SAS3D calculations, eliminating the need for coolant temperature calculations.

A considerable difficulty in discussing fuel pin failure is the uncertainty in the properties of irradiated cladding, in this case 20% CW 316 stainless steel. Failure criteria adopted here, although of uncertain validity, should at least be useful for comparative purposes. One of the criteria, which has

commonly been used[2], is a life fraction rule based on the HEDL Dorn Parameter[3] with failure assumed when the life fraction equals one. Another criterion used is to assume failure when the plastic hoop strain reaches a given value. Three constant values of strain have been chosen here, 0.01%, 1.0%, and 2.0%. The 0.01% value corresponds to the range expected for the fuel adjacency effect according to the theory of DiMelfi and Kramer[4,5]. This effect would not be expected to be applicable for clad failure temperatures below about 1000 K because the fuel creep rate becomes very small and intergranular crack growth, on which the effect is believed to depend, becomes insignificant[4,5]. For the same reason a life fraction rule, also applicable for intergranular creep-type failures, would not be expected to have much validity in the low temperature region[2]. The value of 1.0% for failure strain was chosen to illustrate how failure conditions would be changed for a clad of relatively high ductility. For 2.0% plastic strain runaway plastic strain is imminent; this represents an extreme failure condition.

Another strain failure condition adopted was based on the HEDL correlations presented in Ref. 6. Correlations were given for clad heating rates of 5.6 K/s and 111 K/s. Actually, the heating rates for the LOF-TOP cases studied here were in the range 300-500 K/s, but the 111 K/s correlation has been applied even so. It was also necessary to extrapolate this correlation beyond the stated range of validity, 1311 K, in some cases. For the TOP cases, in which the heating rate was around 25 K/s, values midway between the 5.6 K/s and 111 K/s values were used. Clad failure plastic hoop strain values resulting from this process are given in Tables II and III; they are mostly in the range 0.1-0.2%. Note that irradiation effects tend to saturate at a clad fluence of about 5×10^{22} n/cm^2, the range relevant here, for both Dorn and strain criteria.

There is a good deal of scatter in the HEDL failure strain data for fueled cladding. In some cases failure strains are very small, in agreement with the DiMelfi-Kramer theory, while in other cases the failure strain ranges up to the order of 1%. Evidently all the factors affecting the fuel adjacency effect are not well understood yet. In any case, the present study at least gives an idea of what the effect of these variations in clad ductility on accident scenarios might be.

Clad stress-strain relations in FPIN2 are based on the theory of DiMelfi and Kramer[7] and irradiation hardness parameters assumed here are consistent with that work.

For each of the three cases, the option available in FPIN2 of either including or excluding fuel creep was exercised. Results for clad failure times for the LOF-TOP cases are given in Table II. Also given are the clad midwall temperatures, midwall hoop stress, plastic hoop strain, and fuel melt fraction at the failure time. The five axial nodes for which these results were obtained are defined in Table II. TOP results are given in Table III. In all cases the choice was made of binding between clad and fuel to prevent relative axial motion with the gap closed, and because the gap was assumed already closed in steady state this binding was effective immediately. For the LOF-TOP cases the power actually tends to drop below normal in the early stages of the transient, leading to temporary opening of the gap. Because this caused problems with FPIN2 at the present state of development the assumed power history was altered to eliminate this drop.

TABLE II. Failure Conditions as Calculated by FPIN2 for a CRBR Fuel Pin

Channel	Failure Criterion	Fuel Creep	LOF-TOP Cases																							
			Failure Time, Axial Node[d]					Clad Midwall Temp, K Axial Node					Clad Midwall Hoop Stress, MPa Axial Node					Clad Midwall Plastic Hoop Strain, % Axial Node					Fuel Melt Fraction Axial Node				
			1	2	3	4	5	1	2	3	4	5	1	2	3	4	5	1	2	3	4	5	1	2	3	4	5
9	Dorn[a]	yes	14.980		15.142	14.605	14.800	896		1383	1197	1282	602		84	147	107	0.26	0.052	0.15	0.04	0.091	0.0		0.26	0.0	0.0
	0.01[b]		14.735	15.155	15.118	14.525	14.720	795	1299	1372	1184	1265	667	84	55	147	98						0.0	0.05	0.17	0.0	0.0
	HEDL[c]		14.900		15.150	15.137	14.905	856		1384	1450	1304	636		92	65	96	0.19		0.29	0.41	0.25	0.0		0.28	0.07	0.0
	1.0[b]				15.181	15.148				1428	1465				75	73									0.38	0.08	
	2.0[b]				15.206	15.156				1481	1476				62	77									0.47	0.10	
	Dorn	no	15.070	14.770	14.460	14.540	14.800	954	926	1041	1185	1282	495	518	362	174	103	0.46	0.26	0.01	0.03	0.01	0.0	0.0	0.0	0.0	0.0
	0.01		14.725	14.570	14.455	14.490	14.715	794	881	1040	1180	1264	656	568	359	151	98						0.0	0.0	0.0	0.0	0.0
	HEDL		14.870	14.700	14.575	14.705	14.915	841	910	1054	1223	1306	599	536	376	146	87	0.20	0.15	0.10	0.19	0.26	0.0	0.0	0.0	0.0	0.0
	1.0				15.166	15.147				1399	1464				84	61									0.33	0.08	
	2.0				15.199	15.158				1466	1479				65	73									0.44	0.10	
14	Dorn	yes		14.950	14.660	14.730	14.920		889	1012	1145	1121		585	410	226	157	0.23	0.29	0.006	0.025	0.07		0.0	0.0	0.0	0.0
	0.01		14.835	14.735	14.675	14.700	14.860	769	865	1014	1140	1211	679	592	421	208	131						0.0	0.0	0.0	0.0	0.0
	HEDL		14.860	14.850	15.2123	14.835	15.005	771	878	1181	1164	1235	673	595	342	230	149	0.05	0.17	0.16	0.16	0.21	0.0	0.0	0.35	0.0	0.0
	1.0		15.2125			15.2123	15.2123	844			1300	1320	652			285	207						0.0			0.0	0.0
	2.0					15.2125					1300					289										0.14	
	Dorn	no		15.150	14.645	14.725	14.920		943	1009	1157	1221		509	423	230	154		0.87	0.009	0.026	0.073		0.0	0.0	0.0	0.0
	0.01		14.835	14.720	14.645	14.695	14.860	769	863	1009	1139	1211	678	581	423	208	139						0.0	0.0	0.0	0.0	0.0
	HEDL		14.990	14.825	14.730	14.820	15.000	780	875	1023	1161	1234	636	554	429	293	140	0.24	0.18	0.10	0.15	0.20	0.0	0.0	0.0	0.0	0.0
	1.0		15.211	15.195	15.2127	15.423	15.2126	842	972	1183	1300	1321	595	512	328	188	200						0.0	0.0	0.48	0.10	0.0
	2.0					15.2127					1301					300										0.20	

[a]Life fraction equals one for failure time based on Dorn Parameter.

[b]Clad plastic hoop strain, %.

[c]Clad plastic strain at failure as given in Ref. 5 for clad heating rate of 111 K/s.

[d]Heights in cm of nodes 1-5 respectively are 14.46, 21.78, 21.78, 21.78, 14.46, for a total of 94.26 cm. Respective fractional core heights are 0-0.153, 0.153-0.384, 0.384-0.615, 0.615-0.847, 0.847-1.000. Respective clad fluences in $n/cm^2 \times 10^{-22}$ are 4.5, 5.0, 5.0, 5.0 and 3.9.

TABLE III. Failure Conditions as Calculated by FPIN2 for a CRBR Fuel Pin

Failure Criterion	Fuel Creep	TOP Cases																								
		Failure Time, Axial Node[d]					Clad Midwall Temp, K Axial Node					Clad Midwall Hoop Stress, MPa Axial Node					Clad Midwall Plastic Hoop Strain, % Axial Node					Fuel Melt Fraction Axial Node				
		1	2	3	4	5	1	2	3	4	5	1	2	3	4	5	1	2	3	4	5	1	2	3	4	5
Dorn	yes			11.369	10.540	4.900			975	1053	957			347	244	380			0.002	0.005	0.05			0.41	0.18	0.0
0.01					10.669	4.390				1056	943				260	391									0.19	0.0
HEDL					11.129	10.779				1069	1120				323	231				0.16	0.19				0.24	0.0
1.0					11.899	11.329				1095	1138				303	261									0.32	0.0
2.0						11.629					1150					259										0.02
Dorn	no			5.750	4.880	5.230			873	919	967			517	411	342			0.48	0.28	0.16			0.0	0.0	0.0
0.01		4.480	3.620	3.225	3.425	4.150	717	766	827	884	936	700	632	535	451	377						0.0	0.0	0.0	0.0	0.0
HEDL		5.360	4.260	3.770	3.980	4.860	722	772	836	897	956	675	613	530	434	354	0.17	0.15	0.12	0.11	0.11	0.0	0.0	0.0	0.0	0.0
1.0					11.569					1083					337										0.29	
2.0					11.919					1095					333										0.33	

The trends for clad stress as a function of time obtained in these calculations are typical of those obtained for a fuel pin behavior code with the general modeling assumptions made in FPIN2 and are similar to those described by Kramer and Hughes[2]. At zero or low fuel melt fractions, thermal expansion of solid fuel loads the clad, leading to comparatively high stresses. These stresses eventually fall both because the fuel softens with increasing temperature, and because the clad yields as its stress and temperature increase. Comparison of cases with and without fuel creep assumed show that the drop in clad stress from fuel creep tends to be effective earlier than that from clad yielding. The effect of fuel creep is smaller at the bottom and top of the pin because of the lower fuel temperature. However, loading of the cladding from solid fuel pressure is reduced at the top of the pin because the hotter clad tends to expand away from the fuel. The stress eventually rises again as fuel melting leads to the formation of a central cavity pressurized by fission gas released from melting fuel. This stress from cavity pressure does not become significant until a maximum axial melt fraction of at least 10-20% is attained.

Inspection of the results in Tables II and III indicate that the Dorn parameter criterion usually leads to early failure while solid fuel clad loading is still effective and clad plastic hoop strain is small, so that the results are often similar to those assuming failure at 0.01% strain. The effect of fuel creep is very large for the 10 ¢/s TOP case, as would be expected, particularly in the middle part of the pin. Failure occurs at the top of the core with creep taken into account. With no creep, failure occurs very early from solid fuel loading at or just above the core center. It is not sensible physically to neglect fuel creep, and in any event the safety significance of clad failures in the absence of fuel melting is not clear.

We have generally assumed that fuel ejection and accompanying inpin fuel reactivity effects will not occur until a maximum fuel melt fraction of around 0.40 is attained. This means that unless high clad ductility is assumed, failure from solid fuel expansion would have already occurred over the length of the pin in the LOF-TOP cases. These early failures could influence the locations of fuel ejection later on, but this is not really known. Such an influence would presumably tend to reduce inpin reactivity effects.

For the channel 9 LOF-TOP case, if no fuel creep is assumed, high clad stresses caused by solid fuel loading cause early failure according to both Dorn and strain criteria, unless high clad ductility is assumed. For the case with creep, failure also occurs first from solid fuel loading according to the Dorn criterion and the plastic strain criteria with low ductility. For high ductility failure is delayed until significant cavity pressure develops. The results with fuel creep imply that a positive fuel feedback following pin failure might not develop in this case because of the tendency for failure to occur in the upper part of the core. This result could be affected if the steady-state fuel/clad gap was actually open in the upper part of the pin and closed in the middle part instead of being closed over the entire pin as is assumed here. Large cavity pressures do not develop in the channel 9 case because runaway plastic strain allows a large radial cavity displacement before such presssures can develop.

For the channel 14 LOF-TOP case, because of the lower power, fuel stress relaxation effects come in later and consequently have less effect on pin

failure, particularly for application of the Dorn criterion. The large power rise assumed in this case after 15.20 seconds leads to the development of large cavity pressures and runaway plastic strain in node 4. Lower nodes do not develop large strain because of lower clad temperatures.

B. BIFLO Code Development (P. L. Garner)

Posttest analysis of the sodium flow coastdown experiment performed in a 15-pin bundle in the OPERA Facility has continued, with attention focused on performing a two-dimensional calculation using the BIFLO code. A first step in this analysis is dividing the bundle into three or four regions (BIFLO channels) in such a way as to preserve the important features of the steady-state temperature distribution.

Detailed subchannel-geometry calculations performed with the COBRA-IV code indicate that the design of the 15-pin triangular bundle is, indeed, representative of somewhat more than a one-sixth sector of a 61-pin hexagonal bundle. At a given axial level, the corner of the triangle at Pin 1 should be the hottest; the temperature should decrease as the bundle is traversed radially from Pin 1 to the opposite ("Outer") wall. The largest radial temperature gradient occurs across the two rows of pins nearest the Outer wall. There should be little variation in temperature as the bundle is traversed laterally (parallel to a row of pins) from one Side wall to the other Side wall. The presence of the wire wraps adds a slight asymmetry to the temperature distribution. The design of the bundle is, thus, such that the temperature distribution should be approximately two dimensional (axial and radial) and should be represented adequately in BIFLO using three or four channels: one channel for the region between the Outer wall and the outermost row of pins (Pins 11-15) and another channel for the region between the outermost row of pins and the next-to-outermost row of pins; the rest of the bundle (up through the corner at Pin 1) can be represented using one or two more channels in BIFLO.

The steady-state temperature distribution measured during the experiment differs significantly from the ideal expected distribution in several respects: (1) Temperatures in the vicinity of the corner at Pin 15 and in the center of the bundle (near Pin 5) are hotter than the temperature in the vicinity of the corner near Pin 1. (2) There are significant lateral temperature gradients; in particular, the lateral temperature gradient along the Outer wall is as large as the radial temperature gradient, with temperatures steadily increasing as the bundle is traversed from the corner at Pin 11 to the corner at Pin 15. (3) The locations of the hottest and coldest regions varies somewhat with axial location. The temperature distribution measured in the bundle is really three dimensional; using a BIFLO channel geometry based on the bundle design would not preserve the important features of the measured temperature distribution.

The deviation of the measured temperature distribution from the expected distribution appears to be due to pins and wire wraps having moved out of their design positions. The fact that the walls of the triangular bundle moved outward (with a midwall displacement of 0.13 cm, which is approximately the same distance as the nominal pin-to-pin spacing) sometime prior to the experiment and the posttest discovery that some of the pin-to-pin spacers were missing from Pins 11 and 15 allow for the possibility of pin and wire wrap movement. The posttest examination did not document the positions of the pins and wire wraps; this information may have only been marginally useful, since the thermocouple data give indications that some pins and wraps moved during the transient part of the experiment.

Examination of the thermocouple data indicates that the bundle can be divided into three regions: two hotter regions and one colder region. The two hotter regions are (1) a small region including the corner at Pin 1 and (2) a larger region including the corner at Pin 15, about half the region adjacent to the Outer wall, and extending inward toward the center of the triangle. Neither of these two hotter regions is the hottest region at all axial levels. The two hotter regions are separated from each other by the colder region, which includes the third corner of the bundle (near Pin 11), the other half of the region adjacent to the Outer wall, most of the bundle interior, and both Side walls. Even with this breakdown, there are significant temperature variations within each region and a small amount of overlap in the temperature ranges spanned by the three regions. There are insufficient data available to allow the bundle to be divided into a larger number of regions, which would minimize the intraregion temperature variation and eliminate the interregion temperature overlap. This region division only defines the number of pins per BIFLO channel; the flow area associated with each channel must be treated parametrically since the pin locations are not known. This three-region breakdown is not purely two-dimensional and, thus, violates the assumption in BIFLO that the lateral velocities (defined at the interfaces between channels) are colinear; the significance of this is not known.

A series of BIFLO calculations is being performed which vary the manner in which the total bundle flow area is distributed among the three channels, looking for a flow area distribution which results in the calculation of steady-state temperatures, transient temperatures, boiling initiation time, and void growth rate which are consistent with the experiment results.

II. THREE-DIMENSIONAL CODE DEVELOPMENT FOR CORE THERMAL-HYDRAULIC ANALYSIS OF LMFBR ACCIDENTS UNDER NATURAL CONVECTION CONDITIONS

A2045

A. INTRODUCTION

The objective of this program is to develop computer programs (COMMIX and BODYFIT) which can be used for either single-phase or two-phase thermal-hydraulic analysis of reactor components under normal and off-normal operating conditions, especially under natural circulation. The governing equations of conservation of mass, momentum, and energy are solved as a boundary value problem in space and as an initial value problem in time.

COMMIX is a three-dimensional, transient, compressible flow computer code for reactor thermal-hydraulic analysis. It is a component code and uses a porous medium formulation to permit analysis of a reactor component/multicomponent system, such as fuel assembly/assemblies, plenum, piping system, etc., or any combination of these components. The concept of volume porosity, surface permeability, and distributed resistance and heat source (or sink) is employed in the COMMIX code for quasi-continuum thermal-hydraulic analysis. It provides a greater range of applicability and an improved accuracy than subchannel analysis. By setting volume porosity and surface permeability equal to unity, and resistance equal to zero, the COMMIX code can equally handle continuum problems (reactor inlet or outlet plenum, etc.).

B. COMMIX-1A, COMMIX-1B, Single-Phase Code Development (M. Bottoni, F. F. Chen, H. N. Chi, T. Chiang, H. M. Domanus, R. C. Schmitt, W. T. Sha, V. L. Shah, and J. E. Sullivan)

B.1 Free Surface Boundary

There are many possible approaches for implementing the free surface boundary option in COMMIX-1A. We are using a modified VOF (volume of fraction) approach, in which we assume that (i) free surface in a cell is a step (horizontal) surface, and (ii) no multiple regions of void exist in a flow domain under consideration. To calculate void fraction in a cell having a free surface, we have introduced the following additional parameters:

β_v : Liquid fraction of fluid in a cell

$\beta_x = \beta_y$: Directional surface porosity in x and y (horizontal plane) directions.

$\beta_z = 1$ or 0 : Directional surface porosity in z (vertical) direction.

Because of the horizontal step surface assumption, we have

$$\beta_x = \beta_y = \beta_v .$$

To obtain β_v in a cell containing free surface, we solve the following free-surface conservation equation of mass:

$$\frac{\Delta(\gamma_v \beta_v \rho)}{\Delta t} + \frac{\Delta(\gamma_x \beta_x \rho u)}{\Delta x} + \frac{\Delta(\gamma_y \beta_y \rho v)}{\Delta y} + \frac{\Delta(\gamma_z \beta_z \rho w)}{\Delta z} = 0 \qquad \text{(B.1)}$$

In the finite difference formulation of Eq. B.1, we use the upwind value of β_v for β_x and β_y as defined below.

$$(\beta_x)_{i-1/2} = \begin{cases} (\beta_v)_{i-1} & \text{if} \quad (u)_{i-1/2} > 0 \ , \\ (\beta_v)_{i} & \text{if} \quad (u)_{i-1/2} < 0 \ . \end{cases}$$

$$(\beta_y)_{j-1/2} = \begin{cases} (\beta_v)_{j-1} & \text{if} \quad (v)_{j-1/2} > 0 \ , \\ (\beta_v)_{j} & \text{if} \quad (v)_{j-1/2} < 0 \ . \end{cases}$$

Therefore, the basic free surface, Eq. (B.1), simplifies to

$$\frac{\Delta(\gamma_v \beta_v \rho)}{\Delta t} + \frac{\Delta(\gamma_x \beta_v \rho u)}{\Delta x} + \frac{\Delta(\gamma_y \beta_v \rho v)}{\Delta y} + \frac{\Delta(\gamma_z \beta_z \rho w)}{\Delta z} \ . \qquad \text{(B.2)}$$

For a computational cell in liquid phase region, Eq. (B.1) simplifies to

$$\frac{\Delta(\gamma_v \rho)}{\Delta t} + \frac{\Delta(\gamma_x \beta \rho u)}{\Delta x} + \frac{\Delta(\gamma_y \beta \rho v)}{\Delta y} + \frac{\Delta(\gamma_z \rho w)}{\Delta z} = 0 \ , \qquad \text{(B.3)}$$

because $\beta_y = \beta_z = 1$. For a computational liquid-phase cell which is horizontally surrounded by liquid phase cells, Eq. (B.3), reduces to the standard continuity, e.g.,

$$\frac{\Delta(\gamma_v \rho)}{\Delta t} + \frac{\Delta(\gamma_x \rho u)}{\Delta x} + \frac{\Delta(\gamma_y \rho v)}{\Delta y} + \frac{\Delta(\gamma_z \rho w)}{\Delta z} = 0 \qquad \text{(B.4)}$$

because β_x and β_y are equal to one.

All modifications needed for the free surface option have been implemented in the code. We are now debugging the code by running several simple test problems.

B.2 Generalization of Semi-Implicit/Fully-Implicit Schemes in COMMIX

The present development work for COMMIX-1B computer code is the generalization of semi-implicit and fully-implicit schemes in the momentum equation, energy equation, and the governing equations for turbulent quantities. The mixed treatment for this generalized scheme should be

affected by the convective terms only. The generalized equation for a scalar quantity ϕ is

$$\left(\frac{V_0\rho_0}{\Delta t} - S_{p\phi}\, V_0\right)\phi_0 - \left(\frac{V_0\rho_0^n}{\Delta t} - S_{p\phi}V_0\right)\phi_0^n = \alpha \sum_{\ell=1}^{6} a_\ell(\phi_\ell - \phi_0)$$

$$+ (1-\alpha) \sum_{\ell=1}^{6} a_\ell^n (\phi_\ell^n - \phi_0^n) , \qquad (B.5)$$

where $a_\ell = D_\ell + ||(-1)^{\ell+1} F_\ell, 0||$.

The superscript n represents the quantity evaluated at the previous time step, ρ_0 is the density, V_0 is the volume of the cell, Δt is time step, $S_{p\phi}$ is a source or sink term, and α is a parameter with value 0 (represents semi-implicit) or 1 (fully-implicit).

In the pressure equation, the generalized formulation for the convective term F is

$$F = Au[\alpha\rho + (1-\alpha)\rho^n] . \qquad (B.6)$$

For the fully-implicit formulation, $\alpha = 1.0$, Eq. (B.6) becomes the same as the original formulation for fully-implicit scheme.

The advantage of using this generalized formulation is that one formulation is applicable to fully-implicit scheme, semi-implicit scheme, or a scheme which is partially implicit. Furthermore, it eliminates several subroutines previously used for semi-implicit scheme only. The other benefit is the extension of 2-equation k-ε turbulence modeling and volume-weighted skew-upwind differencing to the semi-implicit scheme with only a little effort. Since the generalized scheme uses the same amount of storage for either semi-implicit or fully-implicit scheme, the user can switch back and forth anytime between these two operating schemes. The switching privilege is very useful when the user encounters a transition from a fast transient to slow transient or vice versa.

B.3 DRACS Analysis Capability

In the current design of the Direct Reactor Auxiliary Cooling System (DRACS), in addition to the in-vessel Na/Nak heat exchanger and Intermediate Heat Exchanger (IHX), a Nak/Air heat exchanger is used to remove the decay heat from the reactor core. In order to analyze this kind of DRACS design, the two fluid option in the COMMIX code has been extended to the three fluid option. Similar to the two fluid option, the simplified properties for the third fluid is used. All the related correlations, needed for the evaluation of the third fluid properties, have to be supplied by the users. The advantage of doing this is that the second and third fluids can be any kind of fluid, not necessarily restricted to Nak and air. Several subroutines involved with the third fluid option have been modified accordingly.

The variable IFHTX is added as a flag to identify how many fluids are involved in a problem. The numerical integer value (0, 1, and 2) of IFHTX has the following meaning:

IFHTX = 0	Single fluid only (default)
= 1	Two fluid option
= 2	Three fluid option

In the heat exchanger specification cards (supplied by the user), an additional input variable is added to identify various fluid regions.

Two additional variables TEMP2 (initial temperature approximation of the second fluid) and TAIR (initial temperature approximation of the third fluid) are also introduced. These variables are used to compute the initial properties of the second and third fluid such as density or viscosity. The reasons to introduce these two additional variables (especially TAIR) is because usually there is a large difference between the initial air temperature (generally room temperature) and in-vessel sodium temperature (generally above 300°C).

When the implementation for the three fluid option is completed, a generic simplified DRACS design will be used to demonstrate the heat removal capability by the natural drift air in the air stack.

C. DEVELOPMENT OF COMMIX-2 (M. Bottoni, H. N. Chi, T. H. Chien, H. M. Domanus, R. W. Lyczkowski, C. C. Miao, W. T. Sha, and J. E. Sullivan)

C.1 Organization of a Combined COMMIX-2 Version with both SM(HEM) [Slip Model and Homogeneous Equilibrium Model as a subcase] and SPM [Separated Phases Model] Options

Both SM(HEM) and SPM program versions have been combined into a unified COMMIX-2 program where an input flag (MODEL=1/2) allows the user's choice between them. We explain briefly the new program organization with reference to the simplified flow diagram shown in Fig. 1:

1. The program control is transferred from the driving subroutine AMAIN to either subroutine TIMSTP or TIMSTS (MODEL=1/2).

2. Before advancing the problem time by one time step, the physical properties of the coolant are calculated in subroutine PHYHEM or PHYSPM. Although not shown in the flow chart, the coolant physical properties are recalculated after updating the enthalpy field (after calling subroutine ENLØØP).

3. In the SPM model, the subroutine SOUVAP is used to calculate the mass of coolant vaporizing or condensing per unit of volume and time, taking into account not only the input power source, but also the contribution arising from pressure oscillations. This calculation is made as explained in the next section of this report.

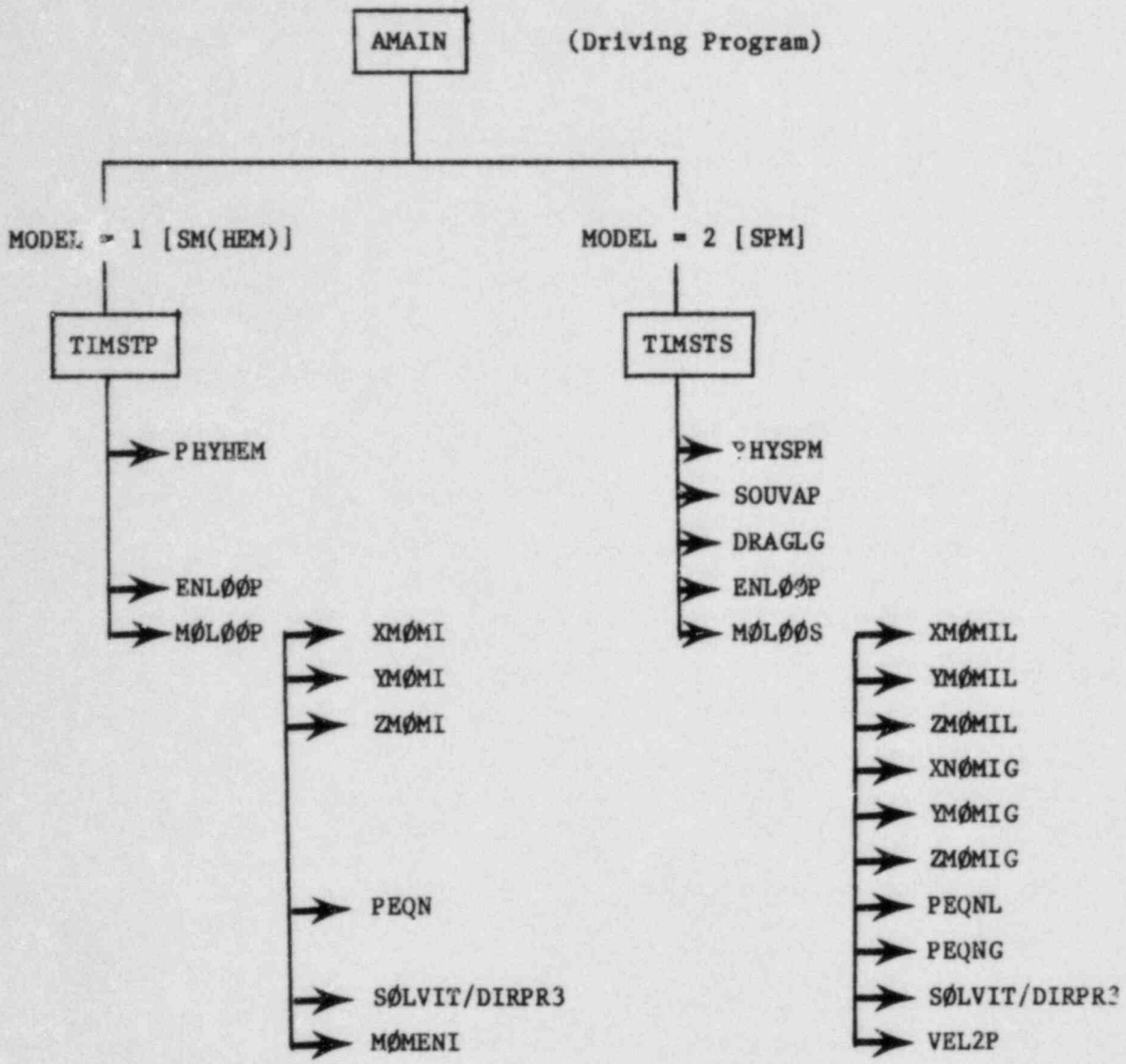

Fig. 1. Scheme showing the main sequence of subroutines called in the SM(HEM) model (if MODEL = 1) and in the SPM (if MODEL = 2) for the solution of the combined or separated momentum equations of the liquid and vapor phases.

The subroutine DRAGLG calculates the drag between the liquid and vapor phases, taking into account different flow regimes.

The two subroutines, SOUVAP and DRAGLG, considered here for completeness, are so far uncompleted. The mass transfer (between the phases) and the momentum transfer represent the strong coupling between the separated momentum equations. In SM(HEM), the mass transfer is not calculated explicitly, while the additional momentum transfer in the two-phase flow region is taken into account by means of the two-phase flow multipliers.

4. Solution of the combined energy equation for the coolant mixture is identical in the two models (subroutine ENLØØP). This implies, however, that in the SPM model, coolant mixture velocities must be calculated (see No. 8).

5. After transferring the program control to either the subroutine MØLØØP or MØLØØS (momentum loop driving subroutines), the explicit terms of the momentum equations of the liquid and vapor coolant (or of the mixture) are calculated. This occurs in subroutines XMØMIL, YMØMIL, ZMØMIL for the liquid phase, in XMØMIG, YMØMIG, ZMØMIG for the vapor phase (in the SPM model), and in XMØMI, YMØMI, ZMØMI for the coolant mixture (in the SM(HEM) model).

6. The coefficients of the Poisson-like equation which describes the pressure field are calculated in subroutine PEQNL for the liquid phase, in PEQNG for the vapor phase (in the SPM model), and in PEQN for the coolant mixture (in the SM(HEM) model). In the case of the SPM model, the two Poisson equations for the pressure (obtained for each phase) are added, thus obtaining a combined Poisson equation. This implies that the assumption of equal pressure gradients in the two phases is made.

7. The numerical solution of the Poisson equation describing the coolant pressure distribution is made likewise in both models using either the iterative solution method (subroutine SOLVIT) or the matrix inversion method (subroutines DIRPR1, DIRPR2, DIRPR3 for 1-D, 2-D, and 3-D problems).

8. The coolant mixture velocity components v_m^i ($i = x, y, z$) are calculated in the subroutine MØMENI (SM(HEM)), while the velocity components of the separated phases v_ℓ^i, v_g^i are calculated in the subroutine VEL2P. These velocity components are related to each other by the equations

$$v_\ell^i = v_m^i - x\left(v_g^i - v_\ell^i\right) \qquad (C.1a)$$

$$v_g^i = v_m^i + (1 - x)\left(v_g^i - v_\ell^i\right) \qquad (C.1b)$$

($i = x, y, z$)

where x is the thermodynamic quality (remember, however, that Eqs. 1a and 1b hold only under the assumption of thermodynamic equilibrium between the phases).

In the SM(HEM), Eqs. 1a and 1b are used to calculate the velocity components of the two phases as though they were flowing separately, because they are needed to calculate the energy and momentum slips between the phases, defined by

$$h_{SL} = x(1 - x) \cdot \rho_\ell \left(h_{gs} - h_{\ell s}\right) \qquad \text{(C.2a)}$$

$$M_{SL} = x(1 - x)\, \rho_\ell \ , \qquad \text{(C.2b)}$$

respectively. In Eqs. 2a and 2b, ρ_ℓ is the liquid coolant density and $h_{\ell s}$ and h_{gs} are the liquid and vapor specific enthalpies on the respective saturation lines.

In the SPM model, either Eq. 1a or Eq. 1b is solved with respect to v_m (after the phase velocity components v_ℓ, v_g have been calculated) because the mixture velocity components are used in the solution of the energy equation for the combined phases (see No. 4).

So far, testing of the two options available, SP(HEM) and SPM, yield the same results in the steady-state and transient single-phase flow calculations. The two-phase SPM model is currently being tested. The next step will consist of the implementation of the subroutines SOUVAP and DRAGLG (see No. 3).

C.2 CALCULATION OF THE MASS OF COOLANT VAPORIZING OR CONDENSING PER UNIT VOLUME AND TIME ($M = kg/m^3 s$)

The mass of coolant transferred from one phase to the other (considered positive by vaporization) is calculated under the assumption of thermodynamic equilibrium between the phases. Thus both phases are assumed to have the same temperature T_S (where the index S refers to saturation conditions). The generalization to unequal phase temperatures is foreseen to be modeled in future program development. We derive the analytical expression of the mass transfer M by vaporization or condensation by generalizing to the three-dimensional case the one-dimensional treatment given in Ref. 8.

The energy equations of the separated phases are given in terms of specific entropy S (J/kg°C) by:

$$\text{(vapor)} \quad \frac{\partial}{\partial t}\left(\alpha_g \rho_g S_g\right) + \nabla \cdot \left(\alpha_g \rho_g S_g \bar{V}_g\right) = Q_g / T_S \ \left(W/m^3\ {}^0C\right) \qquad \text{(C.3)}$$

$$\text{(liquid)} \quad \frac{\partial}{\partial t}\left(\alpha_\ell \rho_\ell S_\ell\right) + \nabla \cdot \left(\alpha_\ell \rho_\ell S_\ell \bar{V}_\ell\right) = Q_\ell / T_S \ . \qquad \text{(C.4)}$$

The heat transferred to each phase is given by

$$Q_g = K_g A_g (T_w - T_S) \quad (W/m^3) \tag{C.5}$$

$$Q_\ell = K_\ell A_\ell (T_w - T_S) \tag{C.6}$$

where K is a wall-to-coolant heat transfer coefficient, A is the wall surface, and T_w is the wall temperature. It can be assumed that $A_g = \alpha_g A$ and $A_\ell = \alpha_\ell A$. However, in the frame of the equal phase temperature model, the assumption can be made that (as long as coolant liquid film wets the wall surface) the heat is transferred only to the liquid phase ($K_g = 0$).

Letting $Q = Q_g + Q_\ell$, summing Eqs. C.3 and C.4 and combining with the continuity equations of both phases

$$\frac{\partial}{\partial t}(\alpha_g \rho_g) + \nabla \cdot (\alpha_g \rho_g \bar{V}_g) = M \tag{C.7}$$

$$\frac{\partial}{\partial t}(\alpha_\ell \rho_\ell) + \nabla \cdot (\alpha_\ell \rho_\ell \bar{V}_\ell) = -M \,, \tag{C.8}$$

one derives

$$M = \frac{Q}{T_S (S_g - S_\ell)} - \frac{1}{S_g - S_\ell}\left[\alpha_g \rho_g \left(\frac{\partial S_g}{\partial t} + u_g \frac{\partial S_g}{\partial x} + v_g \frac{\partial S_g}{\partial y} + w_g \frac{\partial S_g}{\partial z}\right) + \alpha_\ell \rho_\ell \left(\frac{\partial S_\ell}{\partial t} + u_\ell \frac{\partial S_\ell}{\partial x} + v_\ell \frac{\partial S_\ell}{\partial y} + w_\ell \frac{\partial S_\ell}{\partial z}\right)\right] . \tag{C.9}$$

In Eq. C.9 u, v, and w are the velocity components of either phase in the x, y, and z coordinate directions, respectively. The first term in the right-hand side of Eq. C.9 represents the contribution to the mass transfer due to the heat released from the structure walls to the coolant. The second term represents (as it will be proved in the following) the contribution due to pressure oscillations ("flashing").

From the thermodynamic relationships $dq = T \cdot dS = dh - dp/\rho$ (where p and h are the coolant pressure and specific enthalpy, respectively), one derives for either phase and for the three coordinate directions L_j:

$$T_S \frac{\partial S_i}{\partial t} = \frac{\partial h_i}{\partial t} - \frac{1}{\rho_i}\frac{\partial p}{\partial t} \qquad (i = g, \ell) \tag{C.10}$$

$$T_S \frac{\partial S_i}{\partial L_j} = \frac{\partial h_i}{\partial L_j} - \frac{1}{\rho_i}\frac{\partial p}{\partial L_j} \,, \qquad \begin{matrix}(i = g, \ell) \\ (L_j = x, y, z)\end{matrix} \tag{C.11}$$

Equations C.10 and C.11 imply the assumption of a uniform pressure gradient in the two phases (i.e., no pressure gradient between the two phases in the same computational cell). In the present stage of development of the COMMIX-2 program, this assumption allows us to solve a combined Poisson equation for the pressure distribution in the coolant (instead of two Poisson equations for the separated phases). Inserting Eqs. C.10 and C.11 into Eq. C.9 and rearranging, one derives

$$M = \frac{Q}{h_{fg}} - \frac{1}{h_{fg}}\left[\alpha_g\rho_g\left(\frac{\partial h_g}{\partial t} + u_g\frac{\partial h_g}{\partial x} + v_g\frac{\partial h_g}{\partial y} + w_g\frac{\partial h_g}{\partial z}\right)\right.$$

$$+ \alpha_\ell\rho_\ell\left(\frac{\partial h_\ell}{\partial t} + u_\ell\frac{\partial h_\ell}{\partial x} + v_\ell\frac{\partial h_\ell}{\partial y} + w_\ell\frac{\partial h_\ell}{\partial z}\right) - \frac{\partial p}{\partial t}$$

$$\left. - (\alpha_g u_g + \alpha_\ell u_\ell)\frac{\partial p}{\partial x} - (\alpha_g v_g + \alpha_\ell v_\ell)\frac{\partial p}{\partial y} - (\alpha_g w_g + \alpha_\ell w_\ell)\frac{\partial p}{\partial z}\right] \quad (C.12)$$

where

$$h_{fg} = T_S(S_g - S_\ell) \quad (J/Kg) \quad (C.13)$$

is the vaporization enthalpy.

Because on the saturation lines the specific enthalpies are functions of pressure only, we can write:

$$\frac{\partial h_i}{\partial t} = \frac{dh_i}{dp}\frac{\partial p}{\partial t} \qquad (i = g, \ell) \quad (C.14)$$

$$\frac{\partial h_i}{\partial L_j} = \frac{dh_i}{dp}\frac{\partial p}{\partial L_j} \qquad \begin{matrix}(i = g, \ell)\\ (L_j = x, y, z)\end{matrix} \quad (C.15)$$

Introducing Eqs. C.14 and C.15 into Eq. C.12, one derives

$$M = \frac{Q}{h_{fg}} - \frac{1}{h_{fg}}\left\{\frac{\partial p}{\partial t}\left(\alpha_g\rho_g\frac{dh_g}{dp} + \alpha_\ell\rho_\ell\frac{dh_\ell}{dp} - 1\right)\right.$$

$$+ \frac{\partial p}{\partial x}\left[\alpha_g\rho_g u_g\frac{dh_g}{dp} + \alpha_\ell\rho_\ell u_\ell\frac{dh_\ell}{dp} - (\alpha_g u_g + \alpha_\ell u_\ell)\right]$$

$$+ \frac{\partial p}{\partial y}\left[\alpha_g\rho_g v_g\frac{dh_g}{dp} + \alpha_\ell\rho_\ell v_\ell\frac{dh_\ell}{dp} - (\alpha_g v_g + \alpha_\ell v_\ell)\right]$$

$$\left. + \frac{\partial p}{\partial z}\left[\alpha_g\rho_g w_g\frac{dh_g}{dp} + \alpha_\ell\rho_\ell w_\ell\frac{dh_\ell}{dp} - (\alpha_g w_g + \alpha_\ell w_\ell)\right]\right\}. \quad (C.16)$$

If the coolant pressure is constant, the second term at the right-hand side of Eq. C.16, which represents the contribution to the mass transfer from the pressure oscillations ("flashing"), vanishes.

In the limiting case of equal phase velocity (slip ratio H = $|\bar{V}_g|/|\bar{V}_\ell| = 1$), Eq. C.16 reduces to

$$M = \frac{Q}{h_{fg}} - \frac{\rho_m}{h_{fg}}\left[x \cdot \frac{dh_g}{dp} + (1 - x)\frac{dh_\ell}{dp} - \frac{1}{\rho_m}\right] \cdot \left(\frac{\partial p}{\partial t} + u\frac{\partial p}{\partial x} + v\frac{\partial p}{\partial y} + w\frac{\partial p}{\partial z}\right) \tag{C.17}$$

where x is the thermodynamic quality and $\rho_m = \alpha_g\rho_g + \alpha_\ell\rho_\ell$ is the mixture density.

C.3 Debugging of COMMIX-2 SPM

The COMMIX-2 SPM (Separated Phases Model) is being debugged and tested against previous results obtained with the SM(HEM) (Slip Model and Homogeneous Equilibrium Model). So far we have verified that the single phase flow calculation is identical (as it should be) with either model. The testing of the two-phase calculation has been started. Beyond this activity, two further calculations have been added. They are: (i) a calculation of coolant mass and energy imbalance for the separated phases, which will yield a convergence criterion for the two-phase flow calculation and (ii) a global enthalpy balance which includes all media in the definition domain, e.g., coolant, fueled pins, structural materials, etc. Such a global balance should provide an overall check in the consistency of the calculation. These two additions are explained here in detail.

C.4 Calculation of Mass and Energy Imbalances for the Separated Phases

Two subroutines called DNGIJK and DNLIJK have been programmed in COMMIX-2 code for checking the mass and energy balances for the vapor and liquid phases, respectively. At the present stage, the two subroutines are being tested.

Details are described as follows:

C.4.1 Continuity Equation

For vapor phase, the finite-difference form of the continuity equation can be expressed as

$$\frac{V_o\rho'^{n+1}_{og}}{\Delta t} + [0, -F_{1g}] + [0, F_{2g}] + [0, -F_{3g}] + [0, F_{4g}] + [0, -F_{5g}] + [0, F_{6g}] = \frac{V_o\rho'^{n}_{og}}{\Delta t} + [0, F_{1g}] + [0, -F_{2g}] + [0, F_{3g}] + [0, -F_{4g}]$$

$$+ [0, F_{5g}] + [0, -F_{6g}] + M V_o , \qquad (C.18)$$

where $[a,b] = \max(a,b)$ and

$$F_{1g} = (\rho'_g Au_g)_{i-1/2} ,$$

$$F_{2g} = (\rho'_g Au_g)_{i+1/2} ,$$

$$F_{3g} = (\rho'_g Av_g)_{j-1/2} ,$$

$$F_{4g} = (\rho'_g Av_g)_{j+1/2} ,$$

$$F_{5g} = (\rho'_g Aw_g)_{k-1/2} ,$$

$$F_{6g} = (\rho'_g Aw_g)_{k+1/2} ,$$

and M represents the net vapor generation rate. $\rho'_g = \alpha\rho_g$ is the macroscopic vapor density. The vapor mass imbalance is obtained from the difference of the left and right hand sides of Eq. (C.18).

A similar formula for the liquid phase is obtained by replacing

$$\rho'_g = \alpha\,\rho_g \text{ with } \rho'_\ell = (1-\alpha)\rho_\ell$$

α with $(1-\alpha)$

M with -M .

C.4.2 Energy Equation

The energy equations are written for the separated phases under the assumption that

1. The two-phase mixture is in thermal equilibrium, and
2. The net heat fluxes contribute fully to the vaporization of the liquid coolant.

The energy equations which were shown in previous monthly reports can be expressed as

$$\frac{\partial}{\partial t}\left(\rho'_{g,s}h_{g,s}\right) + \nabla\cdot\left(\rho'_{g,s}h_{g,s}\bar{u}_g\right) = \alpha_g\left(\frac{\partial p}{\partial t} + \bar{u}_g\cdot\nabla p\right) +$$

$$+ \nabla\cdot\left(k_{g,s}\alpha_g\nabla T_{sat}\right) + \bar{V}_{gi} + M h_{g,s} + K\left(\bar{u}_\ell - \bar{u}_g\right)^2 \quad (C.19)$$

and

$$\frac{\partial}{\partial t}\left(\rho'_{\ell,s}h_{\ell,s}\right) + \nabla\cdot\left(\rho'_{\ell,s}h_{\ell,s}\bar{u}_\ell\right) = \alpha_\ell\left(\frac{\partial p}{\partial t} + \bar{u}_\ell\cdot\nabla p\right) +$$

$$+ \nabla\cdot\left(k_{\ell,s}\alpha_\ell\nabla T_{sat}\right) + \bar{V}_{\ell i} - Mh_{\ell,s} \quad (C.20)$$

where the subscript s denotes that the physical properties of the fluid are evaluated at the saturation condition. V_{gi} and $V_{\ell i}$ are the internal energy sources arising from viscous dissipation. K in Eq. (C.19) represents the effect of drag dissipation, which is assigned completely to the heating of the vapor.

Equations (C.19) and (C.20) are used for two-phase flow. For the subcooled liquid, only one energy equation is used, i.e.,

$$\frac{\partial}{\partial t}\left(\rho_\ell h_\ell\right) + \nabla\cdot\left(\rho_\ell h_\ell\bar{u}_\ell\right) = \frac{\partial p}{\partial t} + \bar{u}_\ell\cdot\nabla p + \nabla\cdot\left(k_\ell\nabla T_\ell\right) + \bar{V}_{\ell i}$$

$$+ \dot{q}_w + \dot{Q} \quad (C.21)$$

where $\dot{q}_w$ is the net wall heat flux to the liquid. $\dot{Q}$ is the intrinsic heat source of the liquid.

The finite difference equations obtained from the differential equations (C.19) and (C.20) can be expressed as

$$a^h_{og}\cdot\left(h^{n+1}_{g,o}\right)_{sat} - \sum_1^6 a^h_{ig}\cdot\left(h^{n+1}_{g,i}\right)_{sat} = b^h_{og} \quad (C.22)$$

and

$$a^h_{o\ell}\cdot\left(h^{n+1}_{\ell,o}\right)_{sat} - \sum_1^6 a^h_{i\ell}\cdot\left(h^{n+1}_{\ell,i}\right)_{sat} = b^h_{o\ell}\,, \quad (C.23)$$

where

$$a^h_{og} = \frac{\rho'^{\,n+1}_g}{\Delta t}V_o + \left[0_1, -F_{1g}\right] + \left[0_1, F_{2g}\right] + \left[0_1, -F_{3g}\right] + \left[0_1, F_{4g}\right]$$

$$+ \left(0_1, -F_{5g}\right] + \left[0_1, F_{6g}\right]$$

$$+ D_{1g} + D_{2g} + D_{3g} + D_{4g} + D_{5g} + D_{6g}$$

$$a^h_{1g} = [0,\ F_{1g}] + D_{1g}$$

$$a^h_{2g} = [0,\ -F_{2g}] + D_{2g}$$

$$a^h_{3g} = [0,\ F_{3g}] + D_{3g}$$

$$a^h_{4g} = [0,\ -F_{4g}] + D_{4g}$$

$$a^h_{5g} = [0,\ F_{5g}] + D_{5g}$$

$$a^h_{6g} = [0,\ -F_{6g}] + D_{6g}$$

$$b^h_{og} = \frac{(\rho'_{og} h_{og})^n V_o}{\Delta t} + \alpha_{g,o} \frac{P_o^{n+1} - P_o^n}{\Delta t} V_o$$

$$+ \alpha_{g,o} \left\{ \left[0,\ (u_g A)_{i+1/2}\right] P_o - \left[0,\ -(u_g A)_{i+1/2}\right] P_2 \right\}$$

$$- \alpha_{g,o} \left\{ \left[0,\ (u_g A)_{i-1/2}\right] P_1 - \left[0,\ -(u_g A)_{i-1/2}\right] P_o \right\}$$

$$+ \alpha_{g,o} \left\{ \left[0,\ (v_g A)_{j+1/2}\right] P_o - \left[0,\ -(v_g A)_{j+1/2}\right] P_4 \right\}$$

$$- \alpha_{g,o} \left\{ \left[0,\ (v_g A)_{j-1/2}\right] P_3 - \left[0,\ -(v_g A)_{j-1/2}\right] P_o \right\}$$

$$+ \alpha_{g,o} \left\{ \left[0,\ (w_g A)_{k+1/2}\right] P_o - \left[0,\ -(w_g A)_{k+1/2}\right] P_6 \right\}$$

$$- \alpha_{g,o} \left\{ \left[0,\ (w_g A)_{k-1/2}\right] P_5 - \left[0,\ -(w_g A)_{k-1/2}\right] P_o \right\}$$

$$+ \alpha_{g,o} \left\{ (u_g A)_{i+1/2} - (u_g A)_{i-1/2} + (v_g A)_{j+1/2} - (v_g A)_{j-1/2} \right.$$

$$\left. + (w_g A)_{k+1/2} - (w_g A)_{k-1/2} \right\}$$

$$+ \left\{ M \cdot (h_{og})_s + K \left[(u_\ell - u_g)^2 + (v_\ell - v_g)^2 + (w_\ell - w_g)^2 \right] \right\} V_o \,.$$

$$D_{1g} = \alpha_g \left(\frac{k_{g,s}}{c_{pg,s}} \frac{A}{\Delta x} \right)_{i-1/2} \qquad D_{4g} = \alpha_g \left(\frac{k_{g,s}}{c_{pg,s}} \frac{A}{\Delta y} \right)_{j+1/2}$$

$$D_{2g} = \alpha_g \left(\frac{k_{g,s}}{c_{pg,s}} \frac{A}{\Delta x} \right)_{i+1/2} \qquad D_{5g} = \alpha_g \left(\frac{k_{g,s}}{c_{pg,s}} \frac{A}{\Delta z} \right)_{k-1/2}$$

$$D_{3g} = \alpha_g \left(\frac{k_{g,s}}{c_{pg,s}} \frac{A}{\Delta y} \right)_{j-1/2} \qquad D_{6g} = \alpha_g \left(\frac{k_{g,s}}{c_{pg,s}} \frac{A}{\Delta z} \right)_{k+1/2}$$

The coefficients $a_{0\ell}^h$, $a_{1\ell}^h$, $a_{2\ell}^h$, $a_{3\ell}^h$, $a_{4\ell}^h$, $a_{5\ell}^h$, $a_{6\ell}^h$, $b_{0\ell}^h$ and $D_{1\ell}$, $D_{2\ell}$, $D_{3\ell}$, $D_{4\ell}$, $D_{5\ell}$, and $D_{6\ell}$ of Eq. (C.23) are obtained by replacing

index g with ℓ

$$\left\{ M\left(h_{g,o}\right)_{sat} + K\left[(u_\ell - u_g)^2 + (v_\ell - v_g)^2 + (w_\ell - w_g)^2\right] \right\} \text{ with}$$

$$- M\left(h_{o,\ell}\right)_{sat}$$

in the above expressions.

The difference between left and right hand sides of Eqs. (C.22) and (C.23) yields the energy imbalances for both phases. Expressions similar to those of Eq. (C.23) can be obtained for the subcooled liquid energy equation (i.e., Eq. (C.21)) by replacing

α_ℓ with 1

$\left(h_{\ell,i}\right)_{sat}$ with $h_{\ell,i}$ $i = 0, 1, 2, \ldots, 6$

$-M\left(h_{o,\ell}\right)_{sat}$ with $\dot{q}_w + \dot{Q}$.

C.5 Check of Global Enthalpy Balance

It was reported previously that during the two-phase flow calculation, the energy imbalance is generally large with peaks up to some percents of the input power. An attempt to resolve this difficulty is being made by implementing a subroutine called BALNCE to check the energy balance in all media of the definition domain.

The enthalpy balance requires that in the steady state the power supplied corresponds to the sum of the power transported by the coolant and the power lost beyond the boundaries.

In the transient case the temperature increment in every medium must account for the difference between power generation and power lost or transported by the coolant:

$$TPSTD = P_H + DEPT + PSTDST + PLOST$$

where

TPSTD = Total energy stored per unit time.

P_H = The difference between the enthaply flows at outlet and inlet boundaries per unit time.

DEDT = Energy stored in coolant per unit time.

PSTDST = Energy stored in structure per unit time.

PLOST = Energy lost out of boundaries per unit time.

These physical quantities are given by

$$P_H = \left(H_{fluid}\right)_{out} - \left(H_{fluid}\right)_{in}$$

$$H_{fi} = (\rho\ W\ h\ A_f)_i$$

$$H_{fo} = (\rho\ w\ h\ A_f)_o$$

$$DEDT = \sum_{\substack{\text{coolant}\\ \text{cells}}} (\rho\ V_f)\left(h^{n+1} - h^n\right)$$

$$PSTDST = \sum_{\substack{\text{Structural}\\ \text{cells}}} (\rho\ c_p)\ V\left(T_{ST}^{n+1} - T_{ST}^{n}\right)$$

$$PLOST = \sum_{\substack{\text{boundary}\\ \text{cells}}} \left\{ S \cdot h_{out} \cdot \left(T_{\substack{\text{outmost}\\ \text{structure}\\ \text{element}}} - T_{\substack{\text{outer}\\ \text{medium}}} \right) \right\} .$$

The relative error

$$e = \frac{TOTPOW - TPSTD}{TOTPOW} \approx 10^{-3} ,$$

where TOTPOW is the input energy per unit time, gives a measure of the accuracy of the calculation.

For an integrated balance over the time-steps (Δt = DTIME) we compute

SDEDT = SDEDT + DEDT • DTIME

SPSTDS = SPSTDS + PSTDST • DTIME

SPLOST = SPLOST + PLOST • DTIME

STOTPW = STOTPW + TOTPOW • DTIME

For consistency, the percentual error

$$Se = [\,STOTPW - (SDEDT + SPSTDS + SPLOST)]/STOTPW$$

should vanish with increasing time in a quasi-stationary calculation run with constant power and time-independent boundary conditions.

References

1. Physics of Reactor Safety Quarterly Report, January-March 1984, NUREG/CR-3504 Vol. I, ANL-84-35 Vol. I, p. 3.

2. J. M. Kramer and T. H. Hughes, "Comparison and Evaluation of Four Transient Fuel Pin Behavior Codes," Proceedings of Topical Meeting on Reactor Safety Aspects of Fuel Behavior, Sun Valley, Idaho, August 2-6, 1981, p. I-265.

3. G. D. Johnson and C. W. Hunter, "Mechanical Properties of Transient-Tested Irradiated Fast Reactor Cladding," Trans. Am. Nucl. Soc. 30, p. 195 (1978).

4. R. J. DiMelfi and J. M. Kramer, Proc. 6th Int. Structural Mech. Reactor Tech., Div. C 3/3, Paris, France (August 1981).

5. J. M. Kramer and R. J. DiMelfi, "LMFBR Cladding Failure Determined by Simultaneous Integration of Kinematic, Deformation-Rate, and Cracking-Rate Equations," Trans. Am. Nucl. Soc. 44, p. 244 (1983).

6. G. D. Johnson and C. W. Hunter, "Mechanical Behavior of Fast Reactor Fuel Pin Cladding Subjected to Simulated Overpower Transients," HEDL-TME 78-13, June 1978.

7. R. J. DiMelfi and J. M. Kramer, "Modeling the Effects of Fast-Neutron Irradiation on the Subsequent Mechanical Behavior of Type 316 Stainless Steel," J. Nucl. Mat. 89, pp. 338-346 (1980).

8. R. W. Lyczkowski and C. W. Solbrig, "Constitutive Rate Equations for Flowing Phases Flashing at Unequal Velocities and Temperatures," Proc. of ANS Thermal Reactor Safety Meeting, Sun Valley, Idaho, pp. 2-424 to 2-442 (July 31 - August 5, 1977).

Distribution for NUREG/CR-3804 Vol. II (ANL-84-35 Vol. II)

Internal:

C. E. Till
R. A. Scharping
R. Avery
R. J. Armani
T. H. Bauer
I. Bornstein/
A. B. Klickman
C. E. Dickerman
F. E. Dunn
R. A. Valentin/L. Baker
S. H. Fistedis
P. L. Garner
E. Gelbard
H. H. Hummel (5)
Kalimullah
J. M. Kramer
D. H. Lennox
L. G. LeSage
A. P. Olson
D. J. Malloy
P. Pizzica
F. G. Prohammer
D. Rose/A. J. Goldman/
J. F. Marchaterre
R. Sevy
J. J. Sienicki
B. J. Toppel
J. B. van Erp
D. Weber
H. M. Domanus
V. L. Shah
B. C-J. Chen
R. W. Lyczkowski
W. T. Sha
P. I. Amundson/
S. G. Carpenter
M. J. Lineberry
D. H. Shaftman
A. Travelli
ANL Contract File
ANL Patent Dept.
ANL Libraries (2)
TIS Files (3)

External:

USNRC, Washington, for distribution per R7 (250)
DOE-TIC, Oak Ridge (2)
Manager, Chicago Operations Office, DOE
Applied Physics Division Review Committee:
E. L. Draper, Jr., Gulf States Utilities, Beaumont, Tex. 77004
J. F. Jackson, Los Alamos National Lab., P. O. Box 1663, Los Alamos, N. M. 87545
W. E. Kastenberg, U. California, Los Angeles, Calif. 90024
N. J. McCormick, U. Washington, Seattle, Wash. 98195
D. A. Meneley, Ontario Hydro, 700 University Ave., Toronto, Canada M5G 1X6
J. E. Meyer, Massachusetts Inst. Technology, Cambridge, Mass. 02139
A. E. Wilson, Idaho State U., Pocatello, Id. 83209
Components Technology Division Review Committee:
P. Alexander, Flopetrol Johnston Schlumberger, P. O. Box 36369, Houston, Tex. 77236
D. J. Anthony, General Electric Co., 175 Curtner Ave., San Jose, Calif. 95125
A. A. Bishop, U. Pittsburgh, Pittsburgh, Pa. 15261
B. A. Boley, Northwestern U., Evanston, Ill. 60201
F. W. Buckman, Consumers Power Co., 1945 Parnall Rd., Jackson, Mich. 49201
R. Cohen, Purdue U., West Lafayette, Ind. 47907
J. Weisman, U. Cincinnati, Cincinnati, O. 45221
C. Erdman, Texas A&M U., College Station, Tex. 77843
R. Lancet, Atomics International, P. O. Box 309, Canoga Park, Calif. 91304
K. O. Ott, Purdue U., West Lafayette, Ind. 47907

NRC FORM 335 (2-84) NRCM 1102, 3201, 3202

U.S. NUCLEAR REGULATORY COMMISSION

BIBLIOGRAPHIC DATA SHEET

SEE INSTRUCTIONS ON THE REVERSE

1. REPORT NUMBER (Assigned by TIDC add Vol. No., if any)
ANL 84-35 Vol. II
NUREG/CR-3804 Vol. II

2. TITLE AND SUBTITLE
Physics of Reactor Safety Quarterly Report
April-June 1984

3. LEAVE BLANK

4. DATE REPORT COMPLETED
MONTH: August YEAR: 1984

5. AUTHOR(S)
Applied Physics Division
Components Technology Division

6. DATE REPORT ISSUED
MONTH: YEAR:

7. PERFORMING ORGANIZATION NAME AND MAILING ADDRESS (Include Zip Code)
Argonne National Laboratory
9700 S. Cass Avenue
Argonne, IL 60439

8. PROJECT/TASK/WORK UNIT NUMBER

9. FIN OR GRANT NUMBER
A2015
A2045

10. SPONSORING ORGANIZATION NAME AND MAILING ADDRESS (Include Zip Code)
Division of Reactor Safety Research
Office of Nuclear Regulatory Research
U.S. Nuclear Regulatory Commission
Washington, D.C. 20555

11a. TYPE OF REPORT
Quarterly

b. PERIOD COVERED (Inclusive dates)
April-June 1984

12. SUPPLEMENTARY NOTES

13. ABSTRACT (200 words or less)

This quarterly progress report summarizes work done during the months of April-June 1984 in Argonne National Laboratory's Applied Physics and Components Technology Divisions for the Division of Reactor Safety Research in the U.S. Nuclear Regulatory Commission. The work in the Applied Physics Division includes reports on reactor safety modeling and assessment by members of the Reactor Safety Appraisals Section. Work on reactor core thermal-hydraulics is performed in ANL's Components Technology Division, emphasizing 3-dimensional code development for LMFBR accidents under natural convection conditions. An executive summary is provided including a statement of the findings and recommendations of the report.

14. DOCUMENT ANALYSIS - a. KEYWORDS/DESCRIPTORS
LMFBR Safety
Core Disruptive Accident Analysis
CRBR Licensing
Reactor Core Thermal Hydraulics
Natural Convection Core Cooling

b. IDENTIFIERS/OPEN-ENDED TERMS

15. AVAILABILITY STATEMENT
unlimited

16. SECURITY CLASSIFICATION
(This page) unclassified
(This report) unclassified

17. NUMBER OF PAGES

18. PRICE